Soft Matter

Control of Formation of Viscoelastic Droplets and Distribution of Nano-inclusions in Functional Deposition for Lithium-Sulfur Batteries

Journal:	*Soft Matter*
Manuscript ID	SM-ART-06-2019-001212.R1
Article Type:	Paper
Date Submitted by the Author:	18-Jul-2019
Complete List of Authors:	Divvela, Mounica; Cornell University, Robert Frederick Smith School of Chemical and Biomolecular Engineering Zhang, Rui; Cornell University, Robert Frederick Smith School of Chemical and Biomolecular Engineering Zhmayev, Yevgen; Cornell University, Robert Frederick Smith School of Chemical and Biomolecular Engineering Pinge, Shubham; Cornell University, Robert Frederick Smith School of Chemical and Biomolecular Engineering Lee, Jin Hong; Cornell University, Robert Frederick Smith School of Chemical and Biomolecular Engineering Kim, Seung Wan; Cornell University, Robert Frederick Smith School of Chemical and Biomolecular Engineering Joo, Yong Lak; Cornell University, Robert Frederick Smith School of Chemical and Biomolecular Engineering

Control of Formation of Viscoelastic Droplets and Distribution of Nano-inclusions in Functional Deposition for Lithium-Sulfur Batteries

Mounica J. Divvela[a], Rui Zhang[a], Yevgen Zhmayev[a], Shubham Pinge[a], Jin Hong Lee[a], Seung Wan Kim[a], and Yong Lak Joo[a*]

[*]Author to whom all correspondence should be addressed. Electronic mail: ylj2@cornell.edu

[a]*Robert Frederick Smith School of Chemical and Biomolecular Engineering, Cornell University, Ithaca NY, 14853 USA*

Abstract

Electrospray process produces micro/nano droplets for various applications like thin and uniform coatings, drug carriers and mass spectrometry. In this paper, we study the spray processes of viscoelastic jets using simulations and experiments. In discretized modeling, the jet is perturbed with an axisymmetric instability and the growth of this instability causes the jet to break into droplets. For the experiments, the solution of polyvinyl alcohol in water is sprayed and is visualized using a high-speed camera. The droplet size distribution is studied from simulations with experiments for three spray cases: electrospray, air spray, and air-controlled electrospray. Our simulations and experiments reveal that the electric field is effective in reducing droplet size, while air flow offers more jet break-ups and thus a larger number of droplets. As a result, air-controlled electrospray where these two driving forces are synergistically combined leads to a larger number of smaller droplets than electrospray or air spray. Finally, we applied three spray processes to obtain a deposition of sulfur/mesoporous carbon/graphene/polymer binder composites as a lithium sulfur battery cathode and demonstrated that air-controlled electrospray leads to a higher capacity and rate capability than other processes, exhibiting 800 mAh/g at 0.5C and 600 mAh/g at 2C.

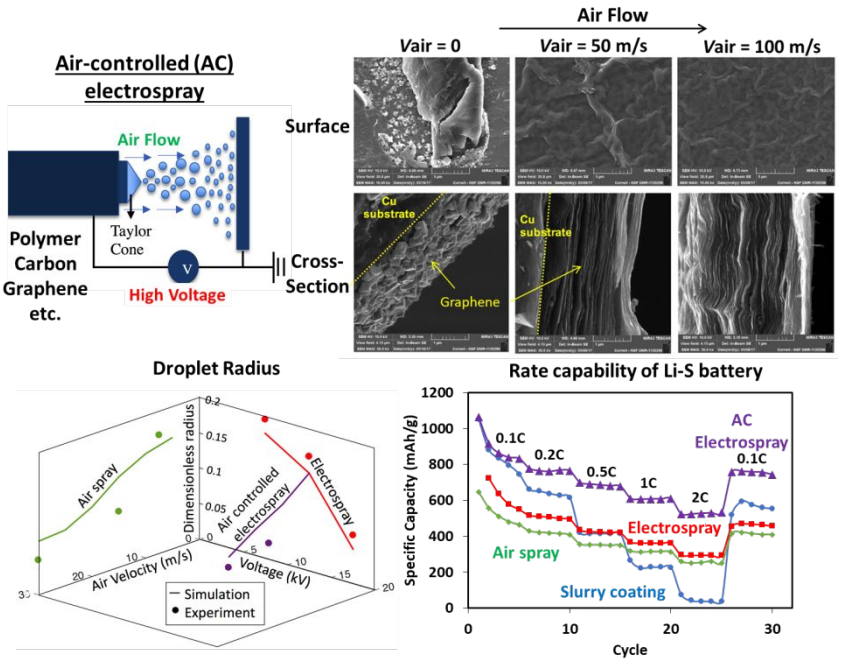

1. Introduction

Electrospray process is used to produce electrically charged droplets of size in micron and submicron range. This process is used in diverse applications like production of thin and uniform coating, nanodroplet and nanostructure production, biomedical engineering, energy storage and mass spectrometry.[1-10] In this process, the electrospraying liquid is pumped out of a needle through a syringe and an electric field is applied between the needle and the collecting plate. When the liquid is released out of the needle the electric field causes the charges to separate inside the liquid meniscus and it takes the shape of a cone at the needle, which is called as Taylor cone.[11] When Taylor cone becomes unstable, depending on the process conditions either jets or droplets are ejected from the cone.[11-14] The axisymmetric instability on the jet results in modulations in the radius of the jet. There have been several classical works on this mode of instability by Plateau and Rayleigh[15] who studied the onset of the instability on a free-falling stream.

In the spray process for viscoelastic jets, the jet extends due to viscoelastic forces and the axisymmetric instability acts on the jet before the break-up. Whereas, in non-viscoelastic liquids,

the atomization of the meniscus at the nozzle is responsible for the formation of droplets. In the electrospray process, the electric field force is responsible for the growth of the instability and the jet breaks into droplets.[16-18] In the air spray process, the external air flow is applied axially to the jet and the air drag accelerates the growth of the axisymmetric instability. In the current work, we look at spray phenomena for the following cases: i) electrospray (only electric field), ii) air spray (only airflow) and iii) air controlled electrospray (airflow and electric field).

There are several theoretical studies on the shape of Taylor cone and electrically driven viscoelastic polymer jets[16-24] but there is less theoretical work on the jet breakup and droplet dynamics in the electrospray process. Among the studies on electrically driven droplets, there have been separate theoretical studies on: i) capillary jet break up under electric field force[25-26], and ii) dynamics of the droplets formed under electric field.[27-28] However, there is no theoretical model combining these two phenomena, as both together are responsible for the electrospray process. Therefore, this work focuses on the breakup of the jet into droplets due to the increase in the growth of the axisymmetric instability, and the dynamics of the droplets as they reach the collecting plate. Combining these two phenomena is difficult with a Eulerian approach as there is a discontinuity in the equations of motion as we shift from jet regime to droplet regime. Therefore, in this work, we use a Lagrangian discretized model as it is suitable to model both the jet breakup and droplet dynamics.[18,24,29-30]

In the discretized model, we consider the liquid jet to be made up of a series of beads attached together with springs. Newton's second law of motion is applied to conserve the momentum. This model has been used in our previous works on centrifugal spinning, and axisymmetric and bending instability study in the electrospinning process.[18,24,29-30] We extend our previous axisymmetric instability[18] work to study the break-up of the jet, which is responsible for the formation of droplets

during the electrospray process. In addition, we incorporate equations of motion for the formed droplets to study their dynamics. In this model, we also model the spray process due to external air flow by incorporating the air drag effects for air spray and air controlled electrospray cases. We also conducted experiments for 5 wt% polyvinyl alcohol in water. The air spray, electrospray, and air controlled electrospray processes are visualized with a high-speed camera. The average radius of the droplets obtained from experiments is compared with simulation results. The surface roughness and efficiency of the coating of PVA/H20 solution on the collector are obtained to study the effect of air flowrate on air controlled electrospray of the solution. We further investigated the effect of additional deformation on the deposition homogeneity and the dispersion of carbon NPs (Carbon Black) in resulting coatings, as it plays a crucial role in energy-storage applications. In addition, we also studied the air controlled electrospray of the solution of graphene oxide dispersion in water to understand the behavior of nano-inclusions in the spray process. Finally, we used the air controlled electrospray process to fabricate cathodes with microporous structures for lithium sulfur batteries. With the application of the air controlled electrospray technique, it is possible to control the morphology of cathode by changing spray parameters and obtain a uniform coating with high sulfur loading. Also, higher sulfur utilization can be achieved through improved electron transfer from low polarization and fast redox reaction kinetics.

2. Electrospray experiment

2.1 Experimental fluids

The spraying solution is 5 wt% of polyvinyl alcohol (PVA) (Mw=25,000 g/mol) in deionized water. The 88% mole hydrolyzed polyvinyl alcohol was purchased from Polysciences, Inc. The

material properties and model parameters of the spinning solution (PVA & water solution) are presented in Table I. The viscosity and relaxation times are obtained from a TA Instruments AR2000 Rheometer with a 20 mm cone steel plate geometry.

TABLE I Material properties and parameters for Gisekus model for 5 wt% of PVA & H_2O solution

Properties	Value
Density (kg/m^3)	964.5
Solution Viscosity (Pa s)	0.026
Surface Tension (N/m)	0.00538
Relaxation Time, λ (s)	0.16
Mobility Factor, α	0.1
Polymer/Solution Viscosity Ratio, β	0.2

The dispersion study of the coating is performed with electrospray and AC electrospray of 3 wt% PVA/H_2O solution with 15 vol.% Carbon Black. Carbon Black (CB) was provided by TIMCAL Graphite & Carbon Super P® Conductive. The graphene oxide solution (2 wt% in water)

was obtained from Dongjin Semichem. This graphene oxide solution was further diluted to 3 wt% solution in water.

For the preparation of spraying solution for lithium sulfur cathodes, carbon/sulfur composite was first prepared by grinding 0.336 g sulfur and 0.084 g Ketjen Black (AkzoNobel) together and heating at 155^{o}C in a for 12 hours to ensure sulfur impregnation. Then the composite was mixed with 0.06 g PAA (Mw =450,000 g/mol, Sigma Aldrich) and 2 g of 6 wt% graphene water solution (ACS Nano). Finally, the mixture was dispersed in 2:8 weight ratio of isopropanol and water to form 6 wt% solution.

2.2 Experimental setup

The experimental setup for the electrospraying is illustrated in Figure 1. The PVA/H2O solution is pumped out of a 16-gauge needle at a flowrate of 0.01 ml/min by using a programmable PHS Ultra syringe pump (Harvard Apparatus). The voltage difference in the spinning gap is obtained with a Gamma High Voltage Research voltmeter. The experiments are conducted for 7.5, 12.5 and 15 kV voltage differences and the spinning distance is at ~ 16 cm. The spinning behavior of the polymer fiber is visualized using a high-speed camera (RedLake MotionPro HS-3 with Nikon MICRO NIKORR 60mm 1:2:8 lens). The images are taken at 1000 frames per second. Finally, the images are digitized using MotionStudio x64 software and are analyzed using ImageJ.

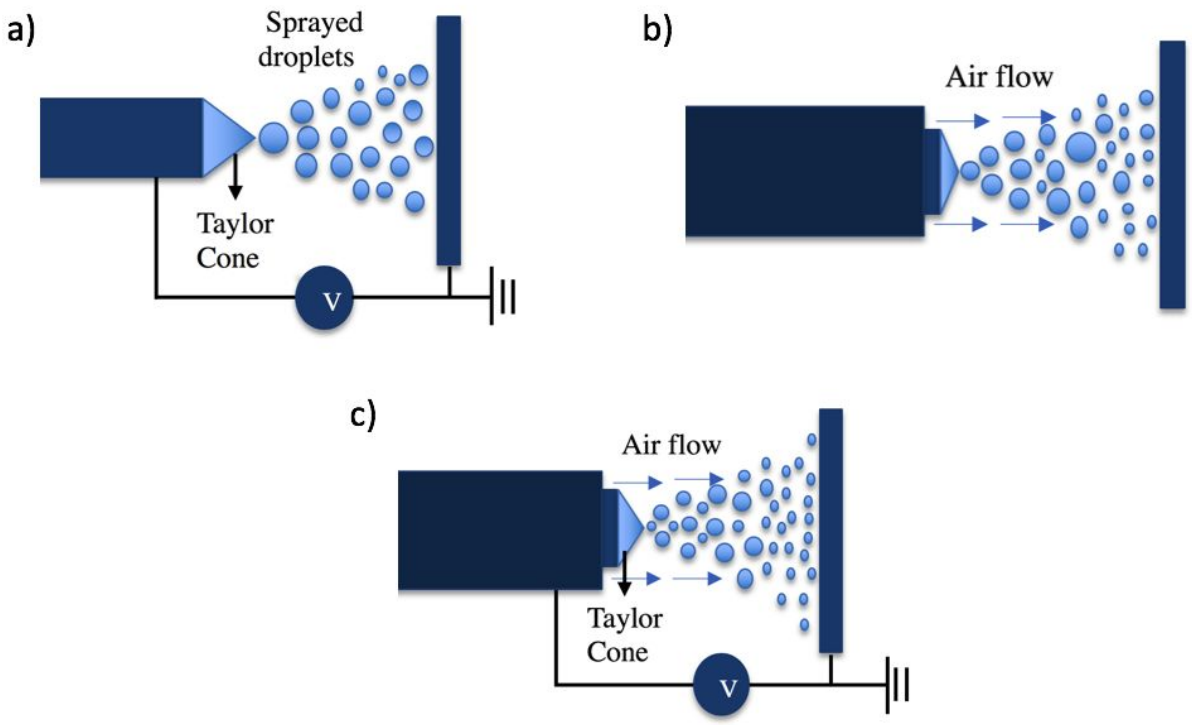

Figure 1. Schematic of a) Electrospray b) Air spray c) Air controlled (AC) electrospray

The coating of 3% PVA/H2O solution containing 15 vol.% Carbon Black is prepared and sprayed via electrospraying and AC electrospraying. The flow rates for electrospraying and AC electrospraying are 0.005 and 0.06 ml min^{-1} respectively, and the electric field is kept constant at 100 kV m^{-1} for both processes. Graphene oxide dispersion in water is sprayed using AC electrospray process at 0.1 ml/min flow rate and voltage difference at 25 kV with spinning distance at 25 cm. Coating morphology and topology are characterized using scanning electron microscopy (Tescan Mira3 FESEM).

Lithium sulfur cathode solution is sprayed onto a carbon coated aluminum foil using a coaxial needle (12-gauge inside, 16 gauge outside). The flow rate and distance are kept at 0.05 ml min^{-1} and 10 cm respectively. The voltage and air pressure are changed to have electrodes sprayed at no electric field (0 kV/ 25 psi), no air (25 kV/ 0 psi) and both the electric field and air (25 kV/ 25 psi). Sample cathodes are used in 2032 coin cell with lithium disk as the anode. Cycling performances are tested with a battery analyzing station (BTS8-MA, MTI) at 0.2 C in a voltage window of 1.8 – 2.8 V.

3. Discretized model

The electrospinning system is modeled using the bead-spring model; the jet is assumed to be a series of beads attached to each other with springs. The modeling approach is similar to the model used previously in the electrospinning and centrifugal spinning systems.[18,24,29-30] The polymer jet that is ejected out of the nozzle is subject to axisymmetric instabilities. This instability further

leads to breaking of the jet into droplets. The modeling procedure used in this work follows from our previous work on axisymmetric instability.[18]

When Eulerian frame of reference is used, it is difficult to have one coordinate system as we shift the frame of reference from the continuous flow of the jet to discrete droplets. However, in the Lagrangian model used in the current study, we can incorporate the equations of motion for both, the continuous polymer jet and the droplets. The beads for the jet are connected with viscoelastic springs and when the jet breaks up and forms droplets, and each droplet is considered as one bead. This model is for predicting the spray process close to the needle so we do not consider the fission of the droplets. Until now all the studies were separately on either the capillary jet breakup or droplet dynamics but this model incorporates both these phenomena in the electrospray process.[25-28]

For the jet, the equations of motion for a bead *'i'* of mass m_i, length l_i, and radius r_i are obtained by applying Newton's second law (Equation (1)). The position vector $\boldsymbol{x_i}$ is obtained from the forces acting on the bead *'i'*, which are surface tension $\boldsymbol{F_{st,i}}$, viscoelastic force $\boldsymbol{F_{v,i}}$, drag force $\boldsymbol{F_{d,i}}$, electric force $\boldsymbol{F_{e,i}}$ and gravitational force $\boldsymbol{F_{g,i}}$. The effects of solvent evaporation are not significant and are not considered in the model as we are studying the jet behavior close to the nozzle.

$$m_i \frac{d^2 \boldsymbol{x_i}}{dt^2} = \boldsymbol{F_{st,i}} + \boldsymbol{F_{v,i}} + \boldsymbol{F_{d,i}} + \boldsymbol{F_{e,i}} + \boldsymbol{F_{g,i}}, \quad (1)$$

The surface tension force and viscoelastic force are obtained from the work by Divvela *et al.*[18,24] The surface tension force has two components: i) capillary force ii) bending force due to the local curvature of the jet. The viscoelastic force is due to the stress from the solvent and polymer; the solvent is a Newtonian fluid, and the polymer stress is obtained from the Giesekus

model. The drag force due to the coaxial air flow is obtained by considering the average of the drag effects on the upstream and the downstream elements. The drag force has two components: i) friction drag due to shear stress on the surface of the jet and ii) pressure drag due to pressure difference in the radial direction of the jet.[30]

The electric force on a bead *'i'* is given from Equation (2). The electric field on the element *i* has two terms: i) voltage gradient with applied voltage difference V_o and spinning length h, and ii) Coulombic interaction with the rest of the beads j with charge q_j at a distance x_{ij} from bead *'i'*. The surface charges are conserved by considering the convection and conduction currents.[18]

$$\boldsymbol{F_{e,i}} = q_i \boldsymbol{E_{e,i}} = q_i \left(\frac{V_o}{h} \boldsymbol{e_z} + \frac{1}{4\pi\epsilon_0} \sum_{j \neq i} \frac{q_j}{{x_{ij}}^3} \boldsymbol{x_{ij}} \right), \tag{2}$$

The bead at the nozzle is disturbed with a normal mode of perturbation with amplitude δ and frequency ω_0. In the context of axisymmetric instability, our approach is similar to that used in the capillary jet breakup study.[25-26] In this study, small fluctuations are applied to the jet boundary condition at the nozzle. The applied perturbation is given in Equation (3), where a_s is the stable jet radius.

$$a = a_s + \delta e^{\omega_0 t}, \tag{3}$$

The simulation is run for different frequencies and amplitudes of the perturbations as given in Equation (3). This perturbation is applied when the bead is introduced at the nozzle exit and we obtain the jet variables by solving Equation (1). This solution will have information on the stable jet and the perturbed variables combined. We calculate the growth rate ω_r of the instability from Equation (4) by measuring the temporal evolution of the perturbation radius, $a_\varepsilon(t)$. Finally, we consider the amplitude δ and frequency ω_0 for which we obtain the maximum growth rate.

$$ln\left(a_\varepsilon(t)\right) = \omega_r t + ln\left(a_\varepsilon(0)\right), \tag{4}$$

The amplitude of the instability increases with time and when this amplitude is equal to the radius of the jet, the jet breaks and forms spherical droplets. Therefore, the jet breakup occurs when $a_\varepsilon(t) = R(t)$, where $R(t)$ is the radius of the jet. The mass, charge, and velocity of the new droplets formed are obtained from conservation of mass (Equation (5)), charge (Equation (6)) and momentum (Equation (7)) equations respectively. In Equations (5 - 7), the subscript '*j*' denotes the indices of all the beads that are in the broken part of the jet.

$$m_i = \sum_j m_j, \tag{5}$$

$$q_i = \sum_j q_j, \tag{6}$$

$$m_i v_i = \sum_j m_j v_j, \tag{7}$$

The equations of motion for these droplets are also obtained from Newton's second law of motion. The forces acting on the beads are aerodynamic drag force ($\boldsymbol{F_{d,i}}$), electric field force ($\boldsymbol{F_{e,i}}$) and gravitational force ($\boldsymbol{F_{g,i}}$). The viscoelastic and surface tension forces are not included in the Equation (8) as we assume that the droplets are rigid spheres.

$$m_i \frac{d^2 \boldsymbol{x_i}}{dt^2} = \boldsymbol{F_{d,i}} + \boldsymbol{F_{e,i}} + \boldsymbol{F_{g,i}}, \tag{8}$$

The air drag force on the droplets is given considering flow on a sphere. For bead *'i'* of radius r_i the drag force is given in Equation (9). Where $\boldsymbol{V_{re}}$, is the relative velocity of the air with respect to the droplet *i*.

$$\boldsymbol{F_{d,i}} = \frac{C_D \pi r_i^2}{2} \rho_{air} \boldsymbol{V_{re,i}} |\boldsymbol{V_{re,i}}|, \quad (9)$$

The drag coefficient C_D (Equation (10)) is obtained from the shear stress acting on the surface of the sphere.[31] The shear stress is calculated from at the velocity profile of the surrounding air on a tiny boundary layer around the surface of the sphere.

$$C_D = \frac{24}{Re_{air}} \left(1 + 0.1104 \sqrt{Re_{air}}\right)^2, \quad (10)$$

The above equation is valid for $Re_{air} < 5000$. Where, $Re_{air} = \rho_{air} |\boldsymbol{V_{re,i}}| d_i / \mu_{air}$ with ρ_{air} as the density of the air, μ_{air} as the viscosity of the air and d_i is the diameter of the droplet.

The electric force acting on the droplets is similar to Equation (2), however, the Coulombic interactions between the droplets and the surface charges of the jet are also responsible for the total electric field force. The details on the implementation and procedure of the discretized modeling to electrically driven jets can be found in previous publications.[16,17, 24]

4. Results and Discussion:

In this section, we studied the spraying process of PVA/H_2O solution and the effect of air flow and voltage is observed. As we used a viscoelastic polymer solution in the experiments, the jet extends due to viscoelastic stress under driving force and then breaks into droplets. The spray process is different for fluids which are not viscoelastic. For non-viscoelastic fluids, the droplets are formed at the nozzle itself due to the atomization of the meniscus (Taylor cone).

In Section 4.1-4.2, the radius of the droplets and the size distribution is obtained for three cases: i) Electrospray ii) Air spray and iii) Air controlled (AC) electrospray. The radius of the droplets obtained from simulations for these three cases is compared with the experimental results. However, the simulation results provide an average radius of the droplets, but the size distributions of the droplets are not obtained. Later, in Section 4.3 the effect of air flow on the surface morphology and the yield of the AC electrospray is studied. The surface morphology formed from the AC electrospray of the solution of graphene oxide dispersion in water, a non-viscoelastic fluid is studied. Finally, in Section 4.4, the three spray processes are applied to coat cathodes for Lithium Sulfur batteries and the electrochemical performance of these batteries is studied.

4.1 Electrospray and Air spray

The experimental conditions used in this section are mentioned in Section 2.1. The electrospray process is studied at 3 different applied voltage differences. The electric field causes extension of the jet from Taylor cone and axisymmetric instability acts on the extended jet. There are two modes of axisymmetric instabilities; the capillary mode and conducting mode.[16-17] In the capillary mode of the instability, the instability grows due to high and low pressure regions caused due to the modulations in the radius of the jet.[16] The low pressure region has larger radius compared to the high pressure region as capillary pressure is inversely proportional to the radius of the jet. As the liquid travels from high pressure to low pressure, the region with larger radius keeps growing and the region with a lower radius keeps shrinking and finally causes the jet to break-up. Whereas in the conducting mode, the modulations on the jet surface lead to modulations on the surface charges of the jet. The Coulombic interactions between these surface charges increase the instability and lead to the jet break-up. In highly conducting polymers, the conducting mode plays

a dominant role in the instability growth rate. With an increase in the electric field, both the capillary pressure and the surface charges of the jet increase due to the formation of thin jets because of jet extension.[17] As the capillary pressure and surface charges are responsible for the jet break-up phenomena, the increase in the electric field leads to an increase in the growth rate of the instability. Therefore, at higher voltages the droplet formation is more rapid, resulting in the formation of a large number of droplets. Also, the formation of thin jets at high voltage leads to smaller size droplets.

In the electrospray process, the jet length is short and the break up occurs near the Taylor cone region. Also, from Figure 2a, the size of the droplets is more consistent as observed from the standard deviation in the droplet size distribution. However, only a fewer number of droplets are formed with the electrospray process. From Figure 2a, we can observe that the radius of the droplets obtained from experiments is comparable to the simulation result.

The experimental result in air spray case is obtained without applying any voltage difference between the nozzle and the collector. The solution is ejected out of the nozzle at flowrate 0.01 ml/min and the air flow is applied coaxially to the jet. The drag force is mainly responsible for the extension of the jet. In this case, as there is no electric field, there is only the capillary mode of the instability and the drag force further accelerates the instability growth rate. The effect of air flow on the droplet size distribution is studied for 3 different air flow rates. From Figure 2b, we can observe that the size of the droplets decreases with the increase in air flow due to the formation of thin jets at high air flow rates. Also, the number of droplets increases with air flow as the instability growth rate also increases with the air flow rates. We also observed that compared to the electrospray process the number of droplets is much higher and the spraying process is more chaotic and rapid for the air spray case. In addition, the droplets formed are not of uniform size

with the air spray case as seen from the standard deviation plot in Figure 2b. From the experimental result for 50 m/s air flow rate, we observe that there are multiple jets formed at the nozzle. However, in the simulations, we assume that only a single jet is ejected out of the nozzle.

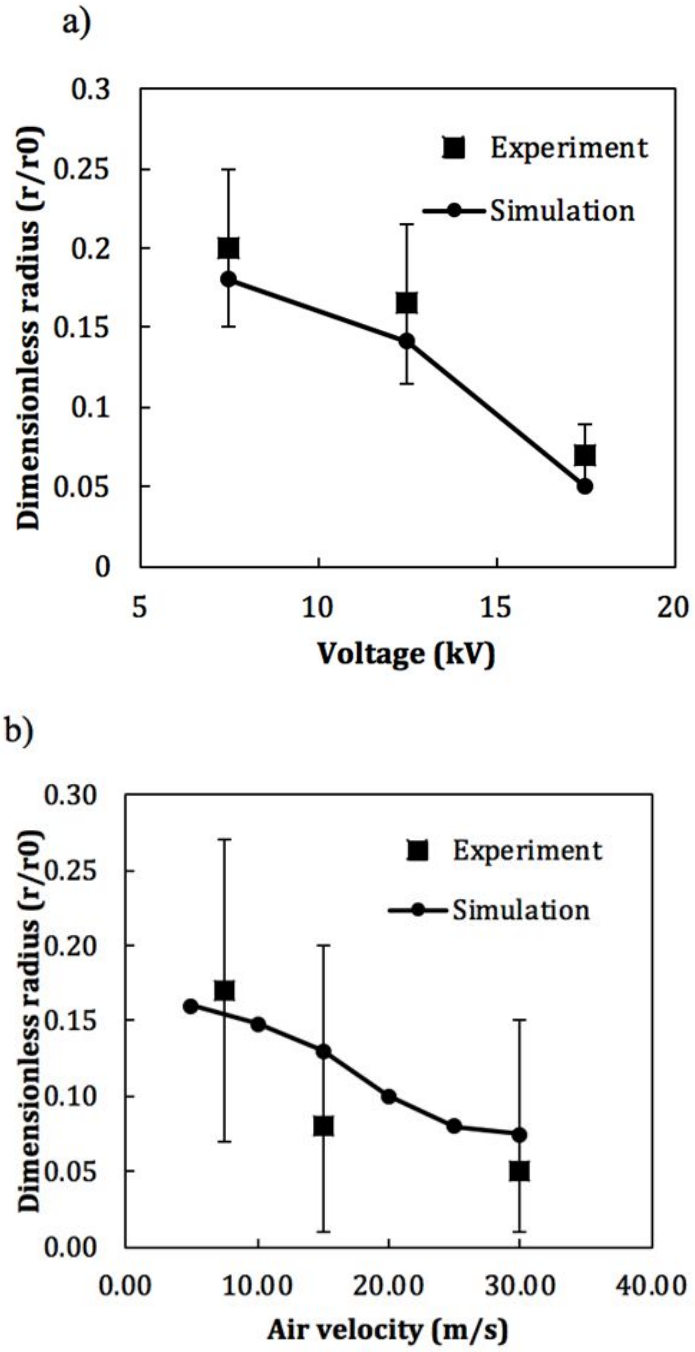

Figure 2. a) Effect of voltage on average droplet radius for electrospray process b) Effect of air velocity on average droplet radius for air spray process

4.2 Air controlled (AC) electrospray

This AC electrospray process is the combination of the electrospray (Section 4.1) and air spray (Section 4.1) processes. The droplet size is more uniform in the AC electrospray process compared to the air spray case due to the application of electric field (Figures 3 and 4). The number of droplets increases with air flow as observed in the air spray case. Therefore, we can observe that the electric field is responsible for the uniformity of the droplets and the air flow is responsible for the formation of a large number of droplets. Also, the mean radius reduces as the air flow increases and the size of the droplets reduce by 65% under the effect of air flow compared to the no air flow case. We also observe that at a higher air flow rate, at 15 m/s, the Taylor cone deforms and ejects multiple jets.

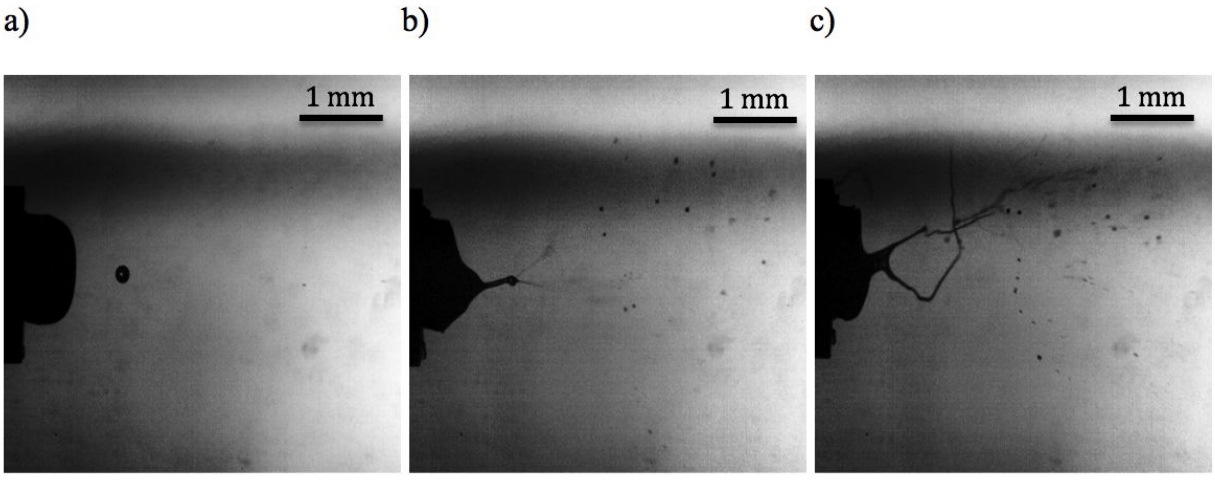

Figure 3. Air controlled electrospray at air flow a) 0 m/s b) 7.5 m/s c) 15 m/s

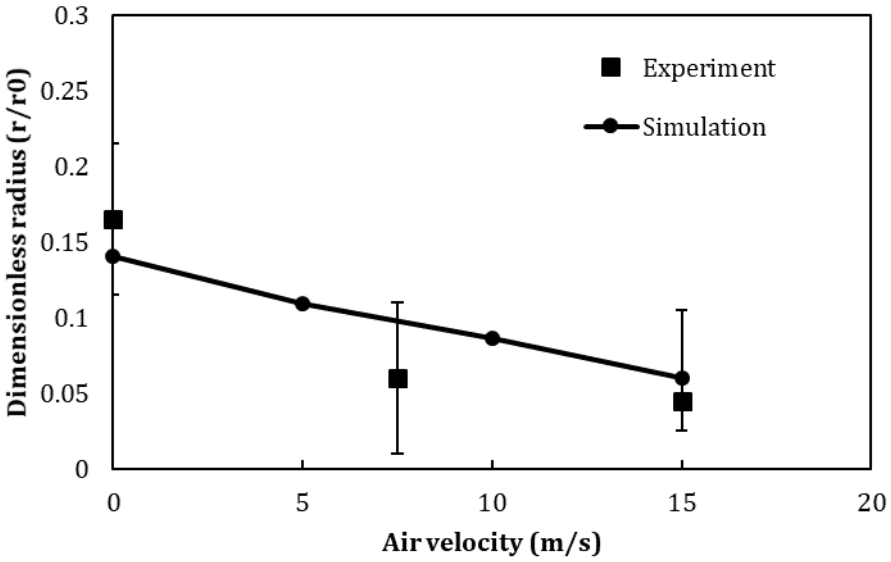

Figure 4. Effect of air flow on average droplet radius for air controlled electrospray process

4.3 Controlling coating topology, morphology and nanoparticle dispersion via AC electrospraying

The surface roughness of PVA/H2O spray is measured through Atomic Force Microscopy (Figure 5a-c) for AC electrospray process at 5 different air flow rates. From Figure 5d, for lower range (0 – 15 m/s) of air flow rates, with an increase in air flow, there is a decrease in surface roughness. However, at a higher air flow rate, at 60 m/s, the surface roughness is increased. The initial decrease in surface roughness is due to the decrease in the size of the droplets sprayed on the substrate as observed in AC electrospray case (Section 4.2). However, at 60 m/s the spray is dry by the time it hits the surface of the collector, and because of which the droplets make a rough coating on the substrate.

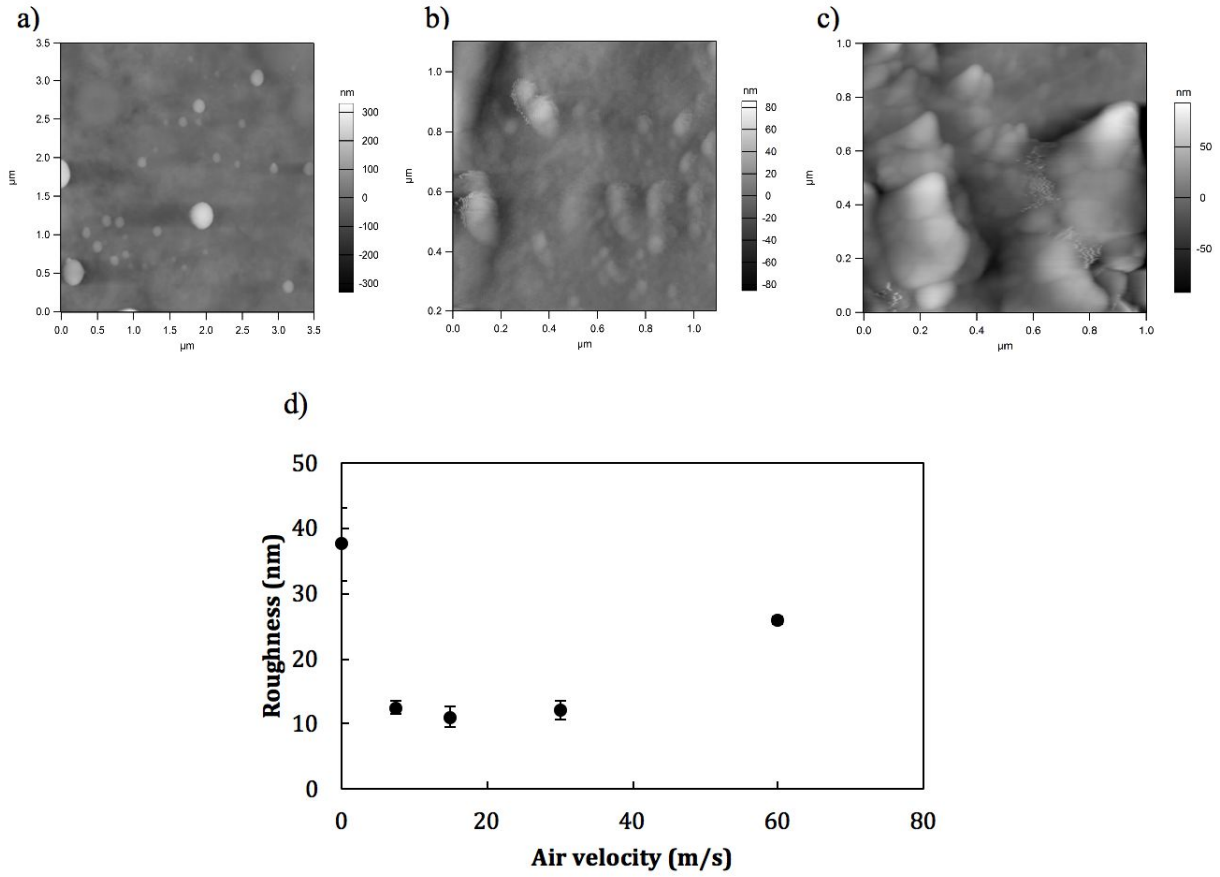

Figure 5. AFM images of AC electrospray surface of PVA/H_2O at air flow a) 0 m/s b) 15 m/s c) 60 m/s and d) Effect of air flow on surface roughness of the coating

The coating efficiency of the spray is also measured for the AC electrospray process at 5 different air flow rates (Figure 6). The coating efficiency is calculated from the ratio of the weight of the coating on the substrate and weight of the polymer in the spinning solution as given in Equation (11). The coating efficiency increases for air flow rates of 0 – 15 m/s due to larger deposition, as the air flow carries the droplets axially towards the substrate. However, at higher air flow rates the

coating efficiency is reduced because of loss in the spray material as the direction of the spray is very non-axisymmetric and chaotic.

$$Coating\ efficiency\ (\%) = \frac{weight\ of\ the\ spray\ coating}{weight\ of\ the\ polymer} \times 100\%, \qquad (11)$$

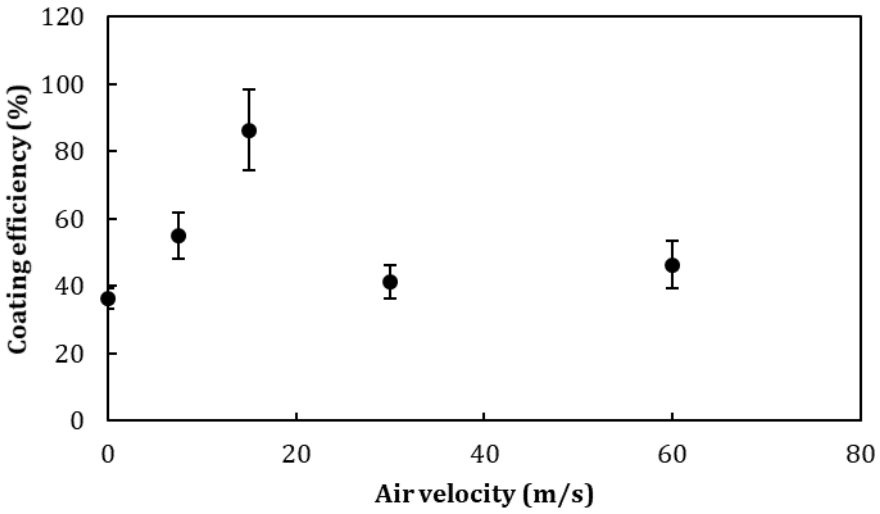

Figure 6. Effect of air flow on coating efficiency of the AC electrospray of PVA/H_2O

Carbon black is added to the PVA solution to investigate the macro-, micro-, and nano-scale morphologies of the PVA-CB coating deposited via AC electrospraying process at different air flows (Figure 7). It is evident from the SEM images (Figure 7) that there is a significant deviation in the size distribution of droplets that are sprayed via conventional electrospray (Figure 7a), ranging from 300 μm (macro-scale) to 50 nm (nanoscale). The solvent evaporation is not precisely controlled in conventional electrospray, which results in deposition of solid polymer particles on the surface, creating rough topology. It can be observed in Figure 7b-d, that with the application of the air flow in AC electrospray, the morphology and topology have significantly improved at all magnifications, due to precise control over atomization and a significant decrease in the droplet

dimensions. It is important to mention, that the number of solid polymer particles on coating surfaces significantly decreased with the increase of the air flow (Figure 7c & d). The polymer droplets are effectively directed towards the substrate by the air flow, therefore, the final solvent evaporation takes place on the surface upon deposition. Extremely high assisting flows result in premature solidification of the droplet, due to forced convection, increasing the number of solid particles on the surface of the coating (Figure 7d). Therefore, AC electrospray can be effectively utilized to precisely control topology and morphology even at the nano scale. This is particularly useful for the development of superhydrophobic coatings, where the control of the surface roughness plays a crucial role and determines wetting angles.[1–3]

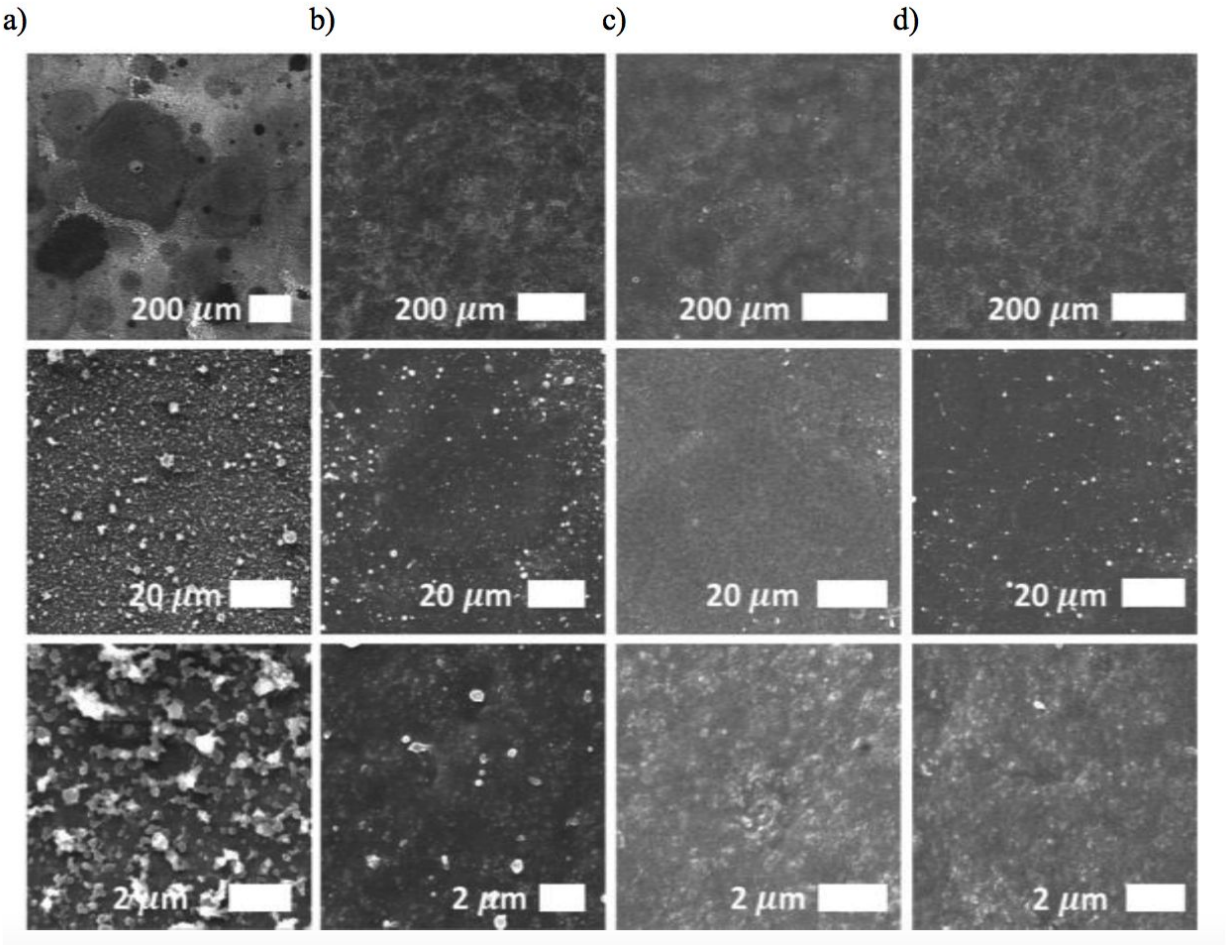

Figure 7. SEM images of macro/micro/nano-topology of 3% PVA solution with CB (15 vol% to PVA) coatings deposited via a) 0 m/s, b) 30 m/s, c) 55 m/s and d) 70 m/s sheath layer air flow AC electrospray.

The AC electrospray of PVA-CB can obtain an electrically conductive coating due to the high electrical conductivity of the carbon powder. However, carbon black cannot be sprayed directly and needs to be sprayed with PVA which acts as a binder to stick to the substrate. In addition, Graphene oxide is electrically conductive and can form uniform coatings using AC electrospray process without the use of PVA (or any binder). Graphene oxide dispersion in water can directly be used to coat copper (Cu) substrate using the AC electrospray process. This solution is non-polymeric, unlike PVA/H2O solution that is used in the experiments discussed in Sections 4.1-4.3. The graphene oxide sheets undergo folding under external forces and therefore, the morphology of the spray surface can give an insight into the droplet formation. When there is no air flow, the spray is very non-uniform and forms discrete particles from the SEM image (Figure 8). However, with the application of air flow rate, the spray forms a film on the substrate. In addition, with an increase in the air flow rate, the spray has fewer wrinkles and a smoother morphology is observed (Figure 8). Furthermore, from the SEM image of the cross-section of the sprayed material, there are no layers formed for no air flow condition. However, layers can be observed when the air flow rate is applied on the spray and the layers are more densely packed for 100 m/s air flow case. This shows that the high air flow rate increases the rate of solvent evaporation of the spray yielding a dry layer of the coating on the substrate before another layer is coated. The layered structure of graphene oxide has been used to fabricate conductive and mechanically stable electrodes in batteries. The multi-layered structure can provide structural integrity and can accommodate large volume changes during the lithiation or delithiation process.

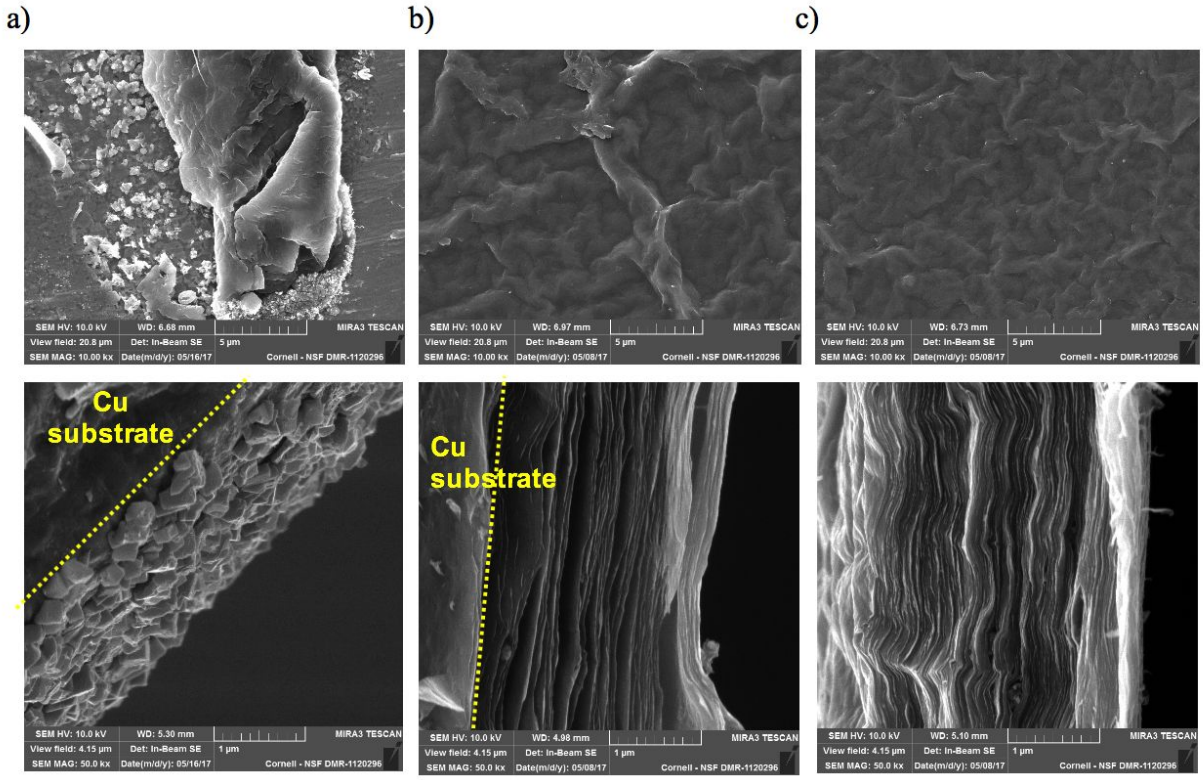

Figure 8. Surface morphology and cross-section of air controlled electrospray of GO at air flow a) 0 m/s b) 50 m/s c) 100 m/s

4.4 Lithium Sulfur battery performance with air controlled electrospray coated electrodes

Li-S batteries are a promising candidate for the next generation of energy storage due to its high theoretical capacity and low cost.[40-41] However, it needs to overcome challenges like the highly insulating nature of sulfur and volume expansion in the battery during discharging. Thus, effective reaction site, conductive pathway, and mechanical stability are necessary to increase the utilization of sulfur. Therefore, in this section, a uniform coated cathode is fabricated using AC electrospray process to improve the capacity and retention of Li-S batteries.

Figure 9 presents the SEM images for the slurry coating, air spray, electrospray, and air controlled electrospray. For slurry coated electrode (Figure 9a), the surface image shows a dense layer with several cracks due to discrete grain boundaries formed during the drying process. The size of the cracks is observed to increase with the sulfur loading and electrode thickness.[42] In the spray techniques (Figure 9b-d), the morphology highly depends on the parameters like flow rate, distance, electric field, and convective air flow. In Figure 9b, the electrospray surface shows a dense surface consisting of inconsistent dark and light color regions. However, air spray electrodes show a more uniform coating as shown in Figure 9c. Furthermore, by combining both, a more porous surface is obtained by air controlled electrospray. The voids and rough surfaces are beneficial as they can accommodate the sulfur expansion and also can enhance the electrolyte uptake.[43] We also note that the porosity of the electrode prepared by air-controlled electrospray with graphene/sulfur filled carbon mixture solution can be controlled by air flow, as alluded in Fig. 8. The typical tap density of the electrode by air-controlled electrospray ranges between 0.2 g/cm^3 to 0.6 g/cm^3, while that prepared by slurry cast is about 0.4 g/cm^3 which is similar to the value reported by Li *et al.*[48]

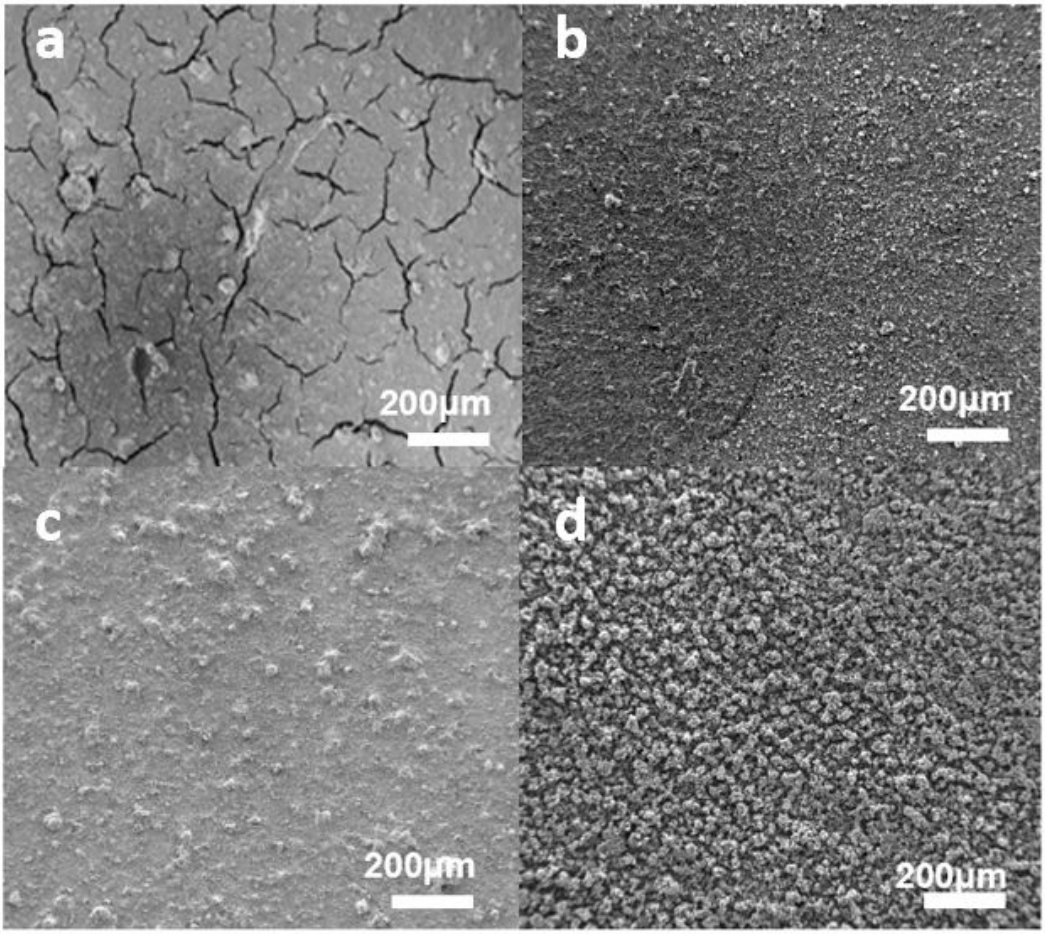

Figure 9. SEM images of cathodes via a) slurry coating, b) electrospray, c) air spray and d) air controlled electrospray

The electrochemical performance of the lithium sulfur battery is measured with four different coated electrodes: i) Slurry coating, ii) Electrospray – Only electric field, iii) Air spray – Only air, and iv) Air controlled electrospray – Both air and electric field. In Figure 10a, the discharge capacity of the electrode coated with air controlled electrospray is higher than the only air and only electric field cases. The higher number of porous micro-size structures formed with both air and electric field provides well-developed pathways to facilitate redox electron transfer and reduce interfacial resistance. It allows a higher conversion rate of lithium polysulfide to favorable chemical compounds for charge storage. Compared to slurry coating electrodes, elimination of

cracks largely increases the mechanical stability, which further results in improved capacity retention.

The rate capability of cells at different C-rates is presented in Figure 10b. As expected, the results followed a similar trend as cyclability. The difference in discharge capacities between the sprayed and slurry coating cells is even more evident at high current densities because the redox reaction kinetics are more significant at high current densities. At a C-rate of 2 C, the air controlled electrospray cell still maintained 49.9 % of its initial capacity, while the retention of slurry coating cathode is only 7.2 %. A discharge capacity of 756.8 mAh g^{-1} is recovered after returning to 0.1 C for air controlled electrospray.

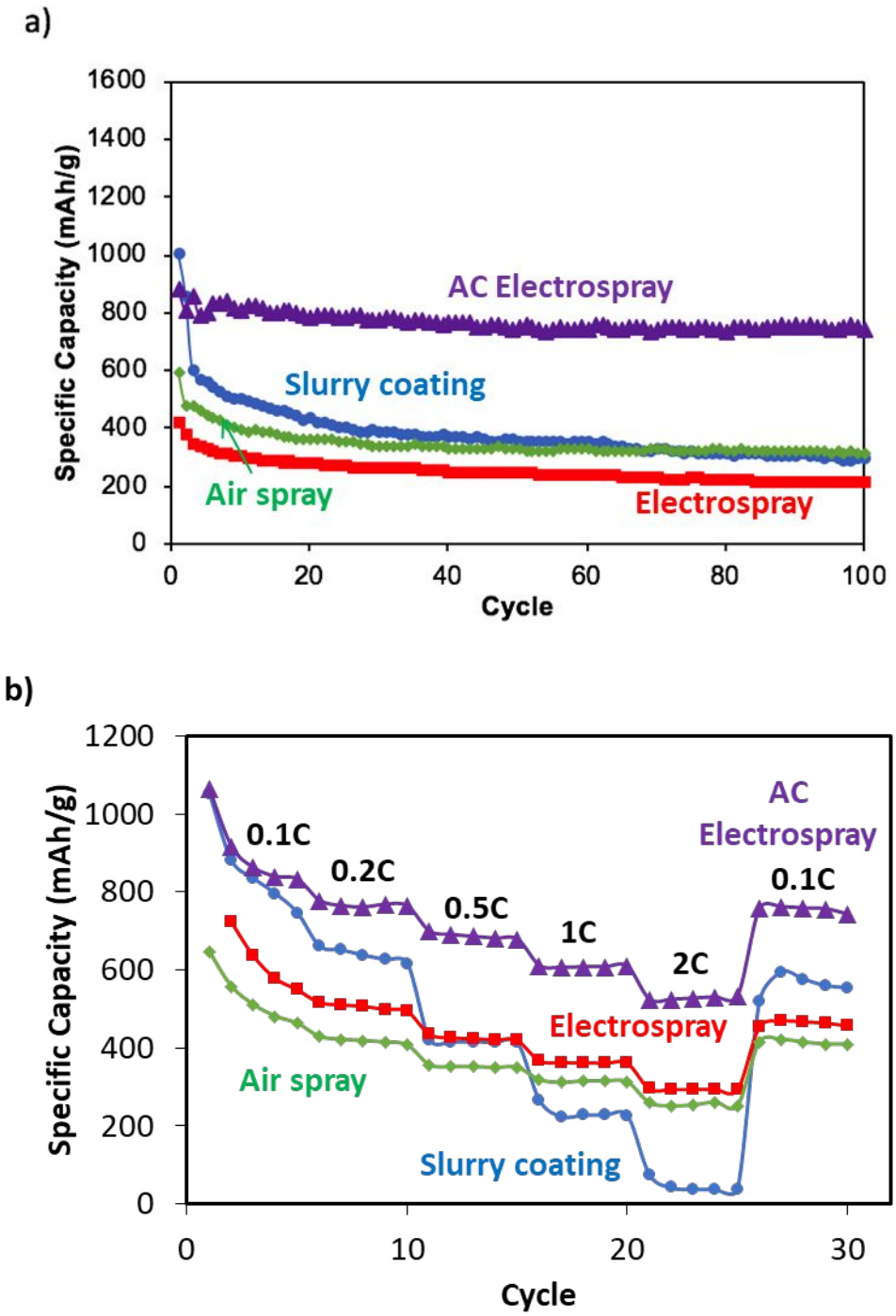

Figure 10. a) Discharge capacity at 0.5 C, and b) Rate capability of lithium sulfur battery cathode fabricated with air controlled electrospray, air spray and electrospray

Conclusions:

The spray behavior of a viscoelastic polymer solution (PVA/H_2O) for air spray, electrospray, and air controlled electrospray cases are studied with simulations and experiments. A discretized model with the bead-spring approach is used for the simulations. The droplet formation from the jet break-up due to axisymmetric instability growth is studied from the model. The average radius of the droplets from simulations is compared with the experiments. The experimental observations are obtained from flow visualization with a high-speed camera and the droplet size distributions for the three spray cases are measured. The electric field is responsible for increasing the uniformity in the droplet size and the air flow rate is responsible for forming a large number of droplets. However, the size of the droplets reduced with the increase in both, the applied electric field and air flow rate. The surface roughness of the AC electrospray material measured from AFM is observed to decrease for lower range (0-15 m/s) of the applied air flow rate but the surface roughness increased at a high air flow rate (60 m/s). Furthermore, for PVA system, we observe a significant improvement in the spatial distribution of Carbon Black active nano-inclusions in the coatings with an increase in the applied air flow. The air controlled electrospray of graphene oxide/water system formed a smoother spray with packed distinct layers at a high air flow rate (100 m/s). The AC electrospray process is used to fabricate uniformly coated Li-S cathodes. The air controlled electrospray coated electrodes demonstrated improved capacity, retention and rate capability. The well-developed structure is efficient not only in providing conductive pathways for sulfur utilization but also for trapping polysulfides.

ACKNOWLEDGMENTS

This work made use of the Cornell Center for Materials Research Shared Facilities which are supported through the NSF MRSEC program (DMR-1719875).

References

[1]E. Burkarter, C. K. Saul, F. Thomazi, N. C. Cruz, L. S. Roman, and W. H. Schreiner, *Surf. Coatings Technol.,* 2007, **202**, 194–198.

[2]J. Bravo, L. Zhai, Z. Wu, R. E. Cohen, and M. F. Rubner, *Langmuir,* 2007, **23**, 7293–7298.

[3]S. T. Yohe and M. W. Grinstaff, *Chem. Commun*., 2013, **49**, 804–806.

[4]Q. Guo, J. P. Mather, P. Yang, M. Boden, and P. T. Mather, *PLoS One,* 2015, **10**, 1–14.

[5]L. T. De Jonge, S. C. G. Leeuwenburgh, J. J. J. P. Van Den Beucken, J. G. C. Wolke, and J. A. Jansen, *Adv. Funct. Mater*., 2009, **19**, 755–762.

[6]M. Valvo, E. García-Tamayo, U. Lafont, and E. M. Kelder, *J. Power Sources,* 2011, **196**, 10191–10200.

[7]C. H. Chen, E. M. Kelder, M. J. G. Jak, and J. Schoonman, *Solid State Ionics,* 1996, **86**, 1301–1306.

[8]L. Wang, H. W. Xu, P. C. Chen, D. W. Zhang, C. X. Ding, and C. H. Chen, *J. Power Sources,* 2009, **193**, 846–850.

[9]M. Yamashita and B. J. Fenn, *The Journal of Physical Chemistry,* 1984, **88**, 4451–4459.

[10]J. B. Fenn, M. Mann, C. K. Meng, S. F. Wong, C. M. Whitehouse, *Science* 1989, **246**, 64–71.

[11]G.I. Taylor, *Proc. R. Soc. Lond. A,* 1964, **280**, 383–397.

[12]G.I. Taylor, *Proc. of the Royal Society of London A: Mathematical, Physical & Eng. Sci.,* 1965**, 291**, 145-158.

[13]G.I. Taylor, *Proceedings of the RoyalSociety of London A: Mathematical, Physical & Engineering Sciences*, 1969, **313**, 453-475.

[14]A.L. Yarin, S. Koombhongse, D.H. Reneker, *J. Appl. Phys*., 2011**, 90**, 4836-4846.

[15]L. Rayleigh, *Proc. London Math. Soc.,* 1879, **10**, 473.

[16]C. P. Carroll, Y. L. Joo, *J. Non-Newtonian Fluid Mech.,* 2008, **153**, 130-148.

[17]C. P. Carroll, Y. L. Joo, *Phys. Fluids,* 2009, **21**, 103101-102110.

[18]M. J. Divvela, Y.L. Joo, *J. Appl. Physics,* 2017, **121**, 134306.

[19]A.F. Spivak, Y.A. Dzenis, D.H. Reneker, *Mech. Res. Commun.,* 2000, **27**, 37-42.

[20]D.H. Reneker, A.L. Yarin, H. Fong, S. Koombhongse, *J. Appl. Phys.,* 2000, **87,** 4531–4547.

[21]M. M. Hohman, M. Shin, G. Rutledge, M.P. Brenner, *Phys. Fluids,* 2001, **13**, 2201.

[22]J. J. Feng, *J. Non-Newtonian Fluid Mech.,* 2003, **116**, 55-70.

[23]C.P. Carroll, Y.L. Joo, *Phys. Fluids,* 2006, **18**, 053102.

[24]M. J. Divvela, L. M. Shepherd, M. W. Frey and Y. L. Joo, *3D Printing and Additive Manufacturing,* 2018**, 5**, 248-256.

[25]A.L. Yarin, *Free Liquid Jets and Films: Hydrodynamics and Rheology*, Longman Scientific & Technical and Wiley & Sons, Harlow, New York, 1993.

[26]P.P. Bhat, S. Appathurai, M.T. Harris, M. Pasquali, G.H. McKinley, O.A. Basaran, *Nature Physics,* 2010, **6**, 625.

[27]J. Grifoll and J. R.-Llompart, *Journal of Aerosol Science,* 2012, **47**, 78–93.

[28]C. B.-Collado, G.Vidal-de-Miguel, P. M.-L. Sinues, *Sensors and Actuators B: Chemical* **223** 217-225 (2016).

[29]C.P. Carroll, Y.L. Joo, *Journal of Applied Physics,* 2011, **109,** 094315-094319.

[30]M. J. Divvela, A.C. Ruo, Y. Zhmayev, Y.L. Joo, *J. Non-Newtonian Fluid Mech*., 2017, **247,** 62-77.

[31]F. F. Abraham, *Physics of Fluids, 1970,* **13,** 2194–2195.

[32]Y. Zhmayev, S. Pinge, G. Shoorideh, G. L. Shebert, P. Kaur, H. Liu, and Y. L. Joo, *Small,* 2016, **12**, 5543–5553.

[33]S. H. Liao, C. C. Weng, C. Y. Yen, M. C. Hsiao, C. C. M. Ma, M. C. Tsai, A. Su, M. Y. Yen, Y. F. Lin, and P. L. Liu, *J. Power Sources,* 2010, **195,** 263–270.

[34]D. V. Kosynkin, W. Lu, A. Sinitskii, G. Pera, Z. Sun, and J. M. Tour, *ACS Nano,* 2011, **5** 968–974.

[35]D. Duft, T. Achtzehn, R. Müller, B. a Huber, and T. Leisner, *Nature,* 2003, **421**, 128.

[36]V. Kalra, F. Escobedo, and Y. L. Joo, *J. Chem. Phys.,* 2010, **132**, 24901.

[37]M. R. Bockstaller, R. A. Mickiewicz, and E. L. Thomas, *Adv. Mater.,* 2005, **17**, 1331–1349.

[38]G. A. Buxton and A. C. Balazs, *Phys. Rev. E. Stat. Nonlin. Soft Matter Phys.,* 2003, **67**, 031802–031814.

[39]A. K. Khandpur, S. Forster, F. S. Bates, I. W. Hamley, A. J. Ryan, W. Bras, K. Almdal, and K. Mortensen, *Macromolecules*, 1995, **28**, 8796–8806.

[40]N. Deng, W. Kang, Y. Liu, J. Ju, D. Wu, L. Li, B. S. Hassan and B. Cheng, *J. Power Sources,* 2016, **331,** 132–155.

[41]Manthiram A, Fu Y and Su Y-S, *Acc. Chem. Res.,* 2013, **46,** 1125-1134.

[42]Z. W. Seh, W. Li, J. J. Cha, G. Zheng, Y. Yang, M. T. McDowell, P. C. Hsu and Y. Cui, *Nat. Commun.,* 2013, **4,** 1331.

[43]P. Barai, A. Mistry and P. P. Mukherjee, *Extrem. Mech. Lett.,* 2016, **9,** 359–370.

[48]M. Li, Y. Zhang, F. Hassan, W. Ahn, X. Wang, W. W. Liu, G. Jiang and Z. Chen, *J. Mater. Chem. A*, 2017, **5**, 21435.

Air-controlled (AC) electrospray

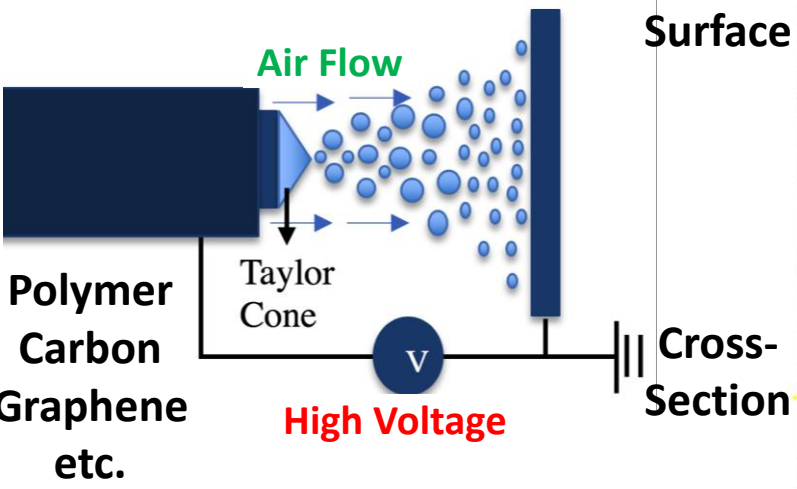

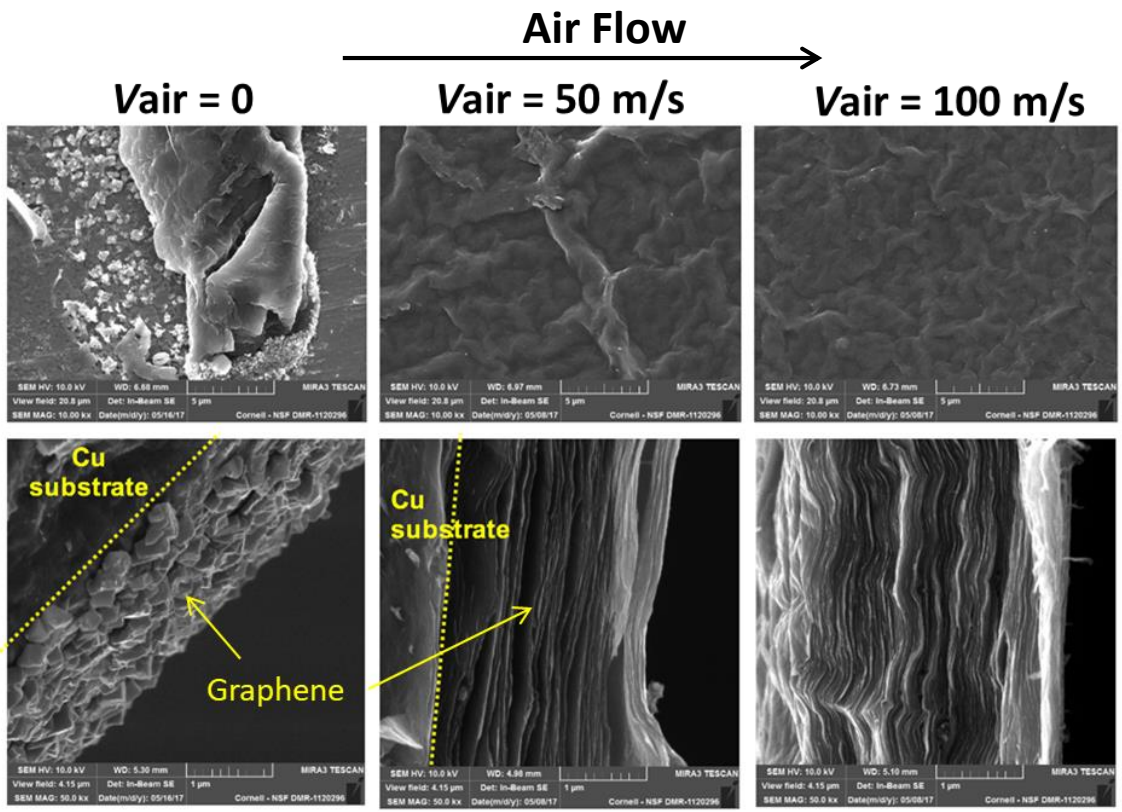

Droplet Radius

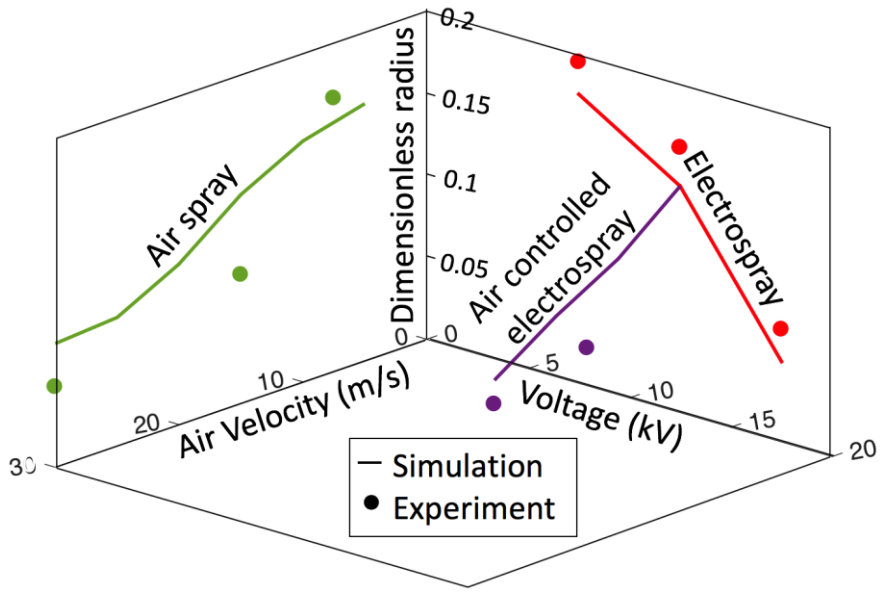

Rate capability of Li-S battery